# nature communications



Article

https://doi.org/10.1038/s41467-025-62388-4

# Flexibility meets rigidity: a self-assembled monolayer materials strategy for perovskite solar cells

Received: 9 January 2025

Accepted: 21 July 2025

Published online: 29 July 2025

Check for updates

Jie Yang<sup>1,10</sup>, Geping Qu<sup>2,3,10</sup> ⊠, Ying Qiao<sup>2,4,10</sup>, Siyuan Cai<sup>2,10</sup>, Jiayu Hu<sup>1</sup>, Shaoyu Geng<sup>1</sup>, Ya Li<sup>1</sup>, Yeming Jin<sup>1</sup>, Nan Shen<sup>1</sup>, Shi Chen **®**<sup>1</sup>⊠, Alex K.-Y. Jen © 3,5,6,7,8 × Zong-Xiang Xu © 2,9 ×

Self-assembled monolayer (SAM) materials have emerged as promising materials for interface engineering in perovskite solar cells. However, achieving an optimal balance between molecular packing density, charge transport efficiency, and defect passivation remains a challenge. In this work, we propose a SAM material design strategy that synergizes flexible head groups with rigid linking groups. Using (4-(diphenylamino)phenyl)phosphonic acid as a model molecule, Compared to traditional materials such as (4-(9H-carbazol-9yl)phenyl)phosphonic acid and (4-(diphenylamino)phenethyl)phosphonic acid, our material generates a high-quality perovskite layer. This design achieves superior energy level alignment, improved hole extraction, and enhanced charge transport efficiency, effectively reducing non-radiative recombination. (4-(diphenylamino)phenyl)phosphonic acid-based device achieve power conversion efficiency of 26.21% and 24.49% for small-(0.0715 cm<sup>2</sup>) and large-area (1 cm<sup>2</sup>), respectively. This work establishes an effective approach to SAM molecular design, providing a clear pathway for improving both the efficiency and long-term stability of perovskite solar cells through interface engineering.

In the past few years, perovskite solar cells (PSCs) have emerged as a focal point of interest within the renewable energy sector, owing to their impressive power conversion efficiencies (PCEs) and the affordability of their production process<sup>1-3</sup>. They have captivated considerable research interest as a cornerstone of next-generation solar cell technology. While the efficiency of PSCs has been steadily converging with that of conventional silicon-based solar cells, the challenges of ensuring long-term stability and mastering interface engineering continue to be pivotal hurdles on the path to commercial viability. Within the realm of PSCs, the optimization of the hole selective layer (HSL) is crucial for not only elevating device efficiency but also for bolstering overall structural stability<sup>4</sup>. Recently, self-assembled monolayers (SAMs) have garnered attention as burgeoning contenders for HSLs, owing to their inherently ultra-thin profiles, exceptional interfacial passivation capabilities, and the versatility of their energy levels, which can be precisely tuned to optimize device performance<sup>5-8</sup>.

<sup>1</sup>Henan Key Laboratory of Quantum Materials and Quantum Energy, School of Future Technology, Henan University, Zhengzhou, China. <sup>2</sup>Department of Chemistry, Southern University of Science and Technology, Shenzhen, Guangdong, China. 3Department of Materials Science and Engineering, City University of Hong Kong, Kowloon, Hong Kong, China. 4Department of Applied Physics, The Hong Kong Polytechnic University, Kowloon, Hong Kong, China. <sup>5</sup>Department of Chemistry, City University of Hong Kong, Kowloon, Hong Kong, China. <sup>6</sup>Department of Materials Science and Engineering, University of Washington, Seattle, WA, USA. 7State Key Laboratory of Marine Pollution, City University of Hong Kong, Kowloon, Hong Kong, China. 8Hong Kong Institute for Clean Energy (HKICE), City University of Hong Kong, Kowloon, Hong Kong, China. 9Guangdong-Hong Kong-Macao Joint Laboratory for Photonic-Thermal-Electrical Energy Materials and Devices, Southern University of Science and Technology, Shenzhen, Guangdong, China. 10 These authors contributed equally: Jie Yang, Geping Qu, Ying Qiao, Siyuan Cai. 🖂 e-mail: gepinggu@cityu.edu.hk; chenshi@henu.edu.cn; alexjen@cityu.edu.hk; xu.zx@sustech.edu.cn

A SAM molecule is generally composed of three distinct components; an anchoring group, a linking group, and a head group. The anchoring groups play a key role in ensuring the adhesion stability of SAMs on the substrate surface, among which the phosphonic acid groups have been proved to be the most robust choice<sup>9</sup>. Meanwhile, it is the judicious design of the linking and head groups that is essential for enhancing charge transport efficiency and facilitating advanced interface engineering within PSCs<sup>4</sup>. In conventional SAM molecules, the linking groups frequently consist of alkyl chains, which feature a non-conjugated, flexible structure. Nonetheless, the inherent insulating nature of these chains frequently acts as a barrier, constraining the efficiency of charge transport<sup>10-12</sup>. This constraint can result in a compromised molecular packing density, which in turn disrupts the orderly arrangement on the substrate surface<sup>13,14</sup>. Consequently, this disturbance can impact the crystallinity and the textual smoothness of the perovskite (PVK) layer<sup>10</sup>, ultimately exerting a discernible influence on the PSCs performance. Investigators have endeavors to substitute conventional alkyl chains with conjugated moieties, including phenyl rings or thiophenes, in a bid to enhance both the intramolecular charge transport efficiency and the molecular packing density<sup>8</sup>. Attaining an optimal balance between the rigidity and flexibility of linking groups, which is essential for realizing both efficient charge transport and structural adaptability, continues to pose a challenge that necessitates additional exploratory research.

The growth of perovskite films strongly depends on the structural configuration of SAM molecule. Both the morphology and crystalline domain size of perovskite films can be precisely tailored through the selection of SAMs<sup>15-17</sup>. Since the head groups of SAM materials serve as critical sites for direct interaction with perovskite precursors, the rational design of head groups becomes a key determinant in optimizing SAM functionality. Aromatic amines, such as carbazole, are among the commonly employed head groups, lauded for their superior hole transport characteristics, which have made them a staple in the field of organic electronics. Nonetheless, the structural rigidity or flexibility of the head group plays a pivotal role in determining the SAM molecules' packing density on the substrate, as well as their overall compatibility with the perovskite layer, thereby influencing the overall performance of PSCs<sup>18</sup>. For instance, the rigid structure of carbazole units leads to a tightly packed configuration at the interface; however, this compact arrangement may exert increased stress on the perovskite layer, with the potential to compromise its crystalline integrity and the stability of the interface19,20. Conversely, the triphenylamine (TPA) structures, characterized by a degree of flexibility, enable tilting and twisting motions, thereby providing a mechanism for stress dissipation within the perovskite layer<sup>21,22</sup>. This flexibility can enhance the crystallization process of perovskite, leading to the development of superior-quality crystals<sup>23</sup>. Moreover, the synergy between the flexibility of the head group and the structure of the linking group plays a pivotal role in determining charge transport dynamics and the characteristics of the interface. Consequently, crafting a balanced design that harmoniously combines rigidity and flexibility within the head group, while ensuring optimal compatibility with the linking group, is essential for optimizing the performance of SAMs.

Building upon the foundation of prior research, the present study conducts a comparative analysis of three distinct SAM molecules—(4-(9*H*-carbazol-9-yl)phenyl)phosphonic acid (PhpPACz), (4-(diphenylamino)phenethyl)phosphonic acid (2PATPA), and (4-(diphenylamino)phenyl)phosphonic acid (PATPA)—in the context of PSC applications. The focus is on elucidating the impact of both rigid and semi-flexible linking groups, as well as the structural attributes of the head groups, on the performance of these devices. Upon comparing PhpPACz with PATPA, it was observed that the semi-flexible TPA head group in PATPA not only facilitated the perovskite crystallization process but also contributed to stress relief, resulting in a lower interfacial defect

density. Additionally, the comparison between 2PATPA and PATPA revealed that the flexibility of the alkyl chain linking group in 2PATPA led to a less compact molecular arrangement, which, in turn, influenced the interfacial potential and charge transport characteristics. Conversely, the rigidity of the phenyl linking group in PATPA enabled a denser molecular packing, which enhanced charge transport capabilities 12. The findings confirm that PATPA, equipped with a rigid phenyl linking group and a semi-flexible TPA head group, delivered the most superior performance in PSCs configured with an Indium-Tin Oxide (ITO)/SAM/PVK/Electron Transporting Layer/Cu structure. Specifically, it achieved an open-circuit voltage ( $V_{\rm OC}$ ) of 1.186 V, a short-circuit current density ( $J_{\rm SC}$ ) of 25.85 mA cm<sup>-2</sup>, a fill factor (FF) of 85.52%, and a PCE of 26.21% (certified 26.26%), thereby underscoring the significance of a balanced design in optimizing SAM performance for advanced PSC technologies.

#### Results

The comprehensive synthesis protocol for PATPA is delineated within the Supplementary Information (Supplementary Figs. 1-6 and Notes 1-4). The spatial configuration and distribution of the SAM molecules, alongside the chemical structures of PhpPACz8, 2PATPA, and PATPA, are depicted in Fig. 1a, b, respectively<sup>24</sup>. PhpPACz is characterized by a highly planar carbazole head group, a stiff phenyl linker, and a phosphate anchor. In distinction to PhpPACz, 2PATPA replaces the carbazole head with a TPA moiety, which confers rotational flexibility, and utilizes a supple alkyl chain as its linker. Both the head and linker of 2PATPA demonstrate a degree of structural flexibility. Conversely, PATPA features a robust phenyl ring as its linker and a rotatable benzene ring as its head group. This architecture combining a flexible head group with a rigid linker is defined as a semi-flexible structure. These structural disparities in the head and linker segments of the three SAM molecules were examined to ascertain their respective influences on device performance.

An exhaustive examination was conducted to elucidate the chemical bonding between the SAM molecules and the ITO substrate. Through X-ray photoelectron spectroscopy (XPS) full-spectrum analysis, a pronounced peak corresponding to phosphorus and a distinct C-P peak at a binding energy of 286.3 eV within the C 1s region were observed, providing definitive evidence of the molecules' secure anchoring onto the ITO surface<sup>25,26</sup> (Supplementary Figs. 7 and 8). To delve deeper into the interaction dynamics between the SAM molecules and the ITO substrate, density functional theory (DFT) calculations were conducted (Supplementary Figs. 9 and 10). The calculated binding energies of -2.35 eV for PhpPACz, -2.43 eV for 2PATPA, and -2.61 eV for PATPA (Supplementary Fig. 10), indicating strong interactions between three SAM molecules to the ITO surface<sup>27</sup>. Moreover, the XPS Sn 3d spectra offered additional corroboration for the observed interactions, revealing a clear trend in binding energy shifts. The Sn 3d peaks for the ITO substrates modified with PhpPACz, 2PATPA, and PATPA all exhibited a shift towards higher binding energies relative to the unmodified ITO (Supplementary Fig. 11).

Ab initio molecular dynamics (AIMD) simulations were conducted to investigate the dynamic behavior of PhpPACz, 2PATPA, and PATPA molecules on the ITO surface (Supplementary Fig. 12). These simulations revealed the distinct stable configurations adopted by SAM molecule on the ITO surface, as shown in Fig. 1c. PhpPACz molecules maintained a vertical orientation with the ITO surface. In contrast, 2PATPA molecules, due to the flexibility of their alkyl chains, arranged themselves in a distorted, nearly parallel configuration with the substrate. PATPA molecule, featuring rigid phenyl linking groups, adopted a tilted orientation on the ITO surface. Based on these simulation results, the alignment and interactions of the three distinct SAM molecule configurations with the ITO contact layer were summarized, as illustrated in Fig. 1d. The AIMD simulations have elucidated that the inclusion of flexible alkyl chains plays a pivotal role in determining the

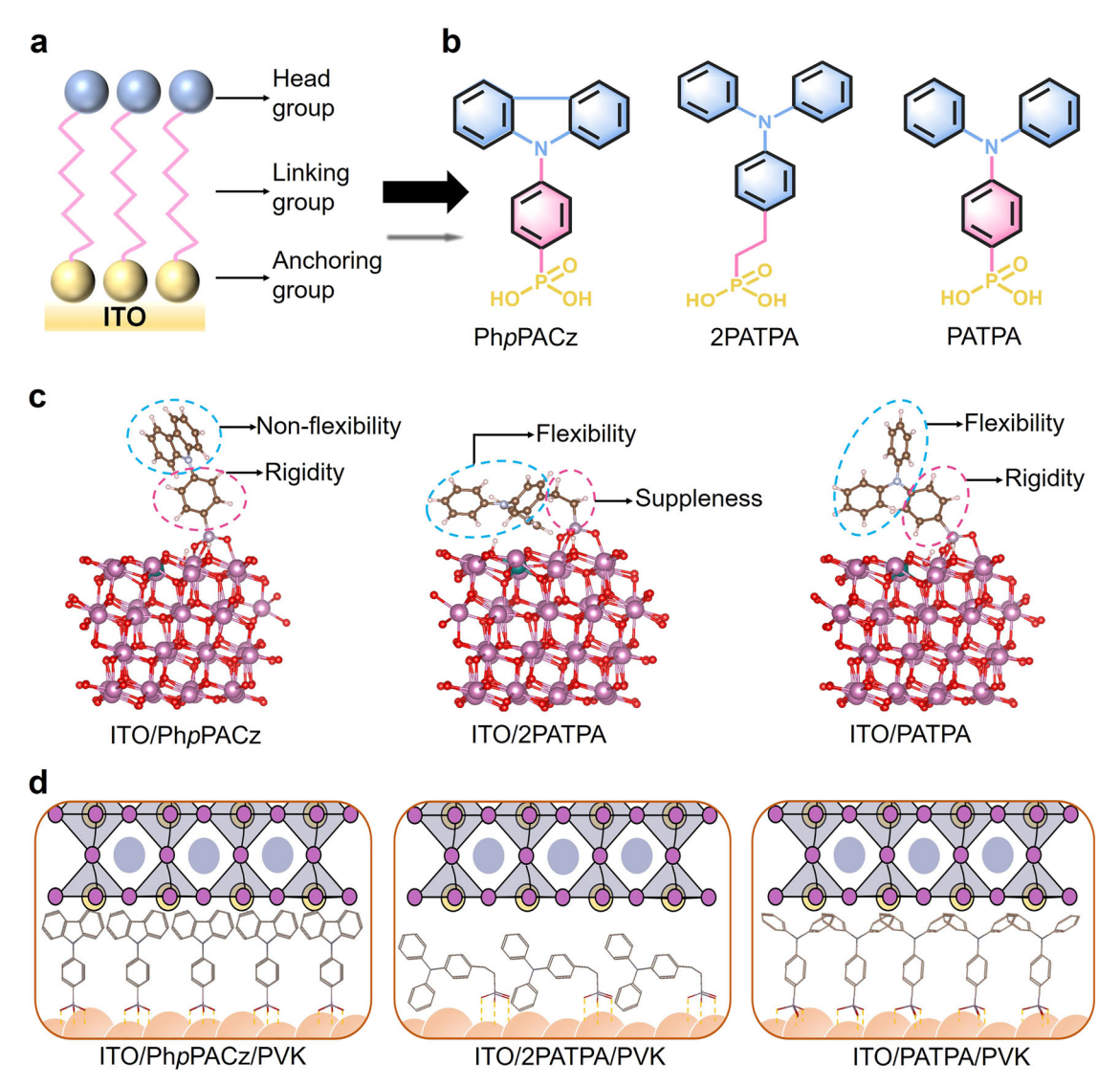


**Fig. 1** | **SAM molecular structures and theoretical simulations. a** Overall configuration distribution of SAM molecule. **b** The Chemical structure of SAM molecules. **c** The final stable configuration of SAM molecules on ITO surface after 10 ps

AIMD simulation. **d** Schematic diagram of ITO/SAM/PVK interface interaction derived from the final stable configuration.

orientation of SAM molecules on the ITO surface. The crux of this investigation lies in the examination and comparison of 2PATPA and PATPA, which are distinguished by their distinct linking groups. To delve deeper into how the rigidity of phenyl linking groups and the flexibility of alkyl linking groups influence charge carrier dynamics, electrostatic potential surface (ESP) calculations were conducted, as illustrated in Fig. 2a.

The findings revealed that the phenyl linking group in PATPA exhibits a pronounced negative charge density, which is visually represented by the more intense red regions in its ESP map. Moreover, the computed molecular dipole moment for PATPA, measured at 2.80 Debye (D), is substantially greater than that of 2PATPA, which stands at 1.31 D (Supplementary Fig. 13). This marked increase in dipole moment implies that when PATPA is employed as a HSL, it is capable of inducing a more robust dipole orientation, with the dipole vector directed from the perovskite layer towards the ITO, thereby enhancing the interfacial charge separation and transport properties<sup>28,29</sup>. This strategically reduces the  $E_{\rm F}$  of the HSL, which in turn promotes efficient charge transfer across the interface. This distinctive attribute offers a theoretical foundation for the improved hole extraction performance<sup>30</sup>. The spectroscopic analysis of ITO/SAMs and the ITO/SAMs/PVK

structures (Supplementary Figs. 14 and 15) revealed that the SAMs did not impart any discernible optical changes.

The electrochemical characteristics of PATPA and 2PATPA were investigated via cyclic voltammetry (CV) techniques. The CV measurements elucidated that the highest occupied molecular orbit (HOMO) energy levels for PATPA and 2PATPA are -5.32 eV and -5.09 eV, respectively (Supplementary Fig. 16 and Supplementary Table 1). These results were further confirmed by calculations, which yielded HOMO levels of -5.52 eV for PATPA and -5.24 eV for 2PATPA, aligning closely with the CV data (Supplementary Fig. 17). Further validation was provided by ultraviolet photoelectron spectroscopy (UPS) analysis, which indicated that the valence band maximum (VBM) for PATPA-modified ITO is -5.41 eV, lower than that for 2PATPAmodified ITO, which is -5.05 eV. In addition, the UPS investigation of the perovskite material revealed a VBM of -5.48 eV (Supplementary Fig. 18 and Supplementary Table 2). The comparative analysis indicated that the energy level misalignment between the VBM of PATPAmodified ITO and the perovskite was 0.07 eV, which is substantially less than 0.43 eV offset measured for the 2PATPA counterpart. In contrast, the VBM of PhpPACz is actually 0.27 eV shallower than the perovskite. This marked improvement in energy level alignment has

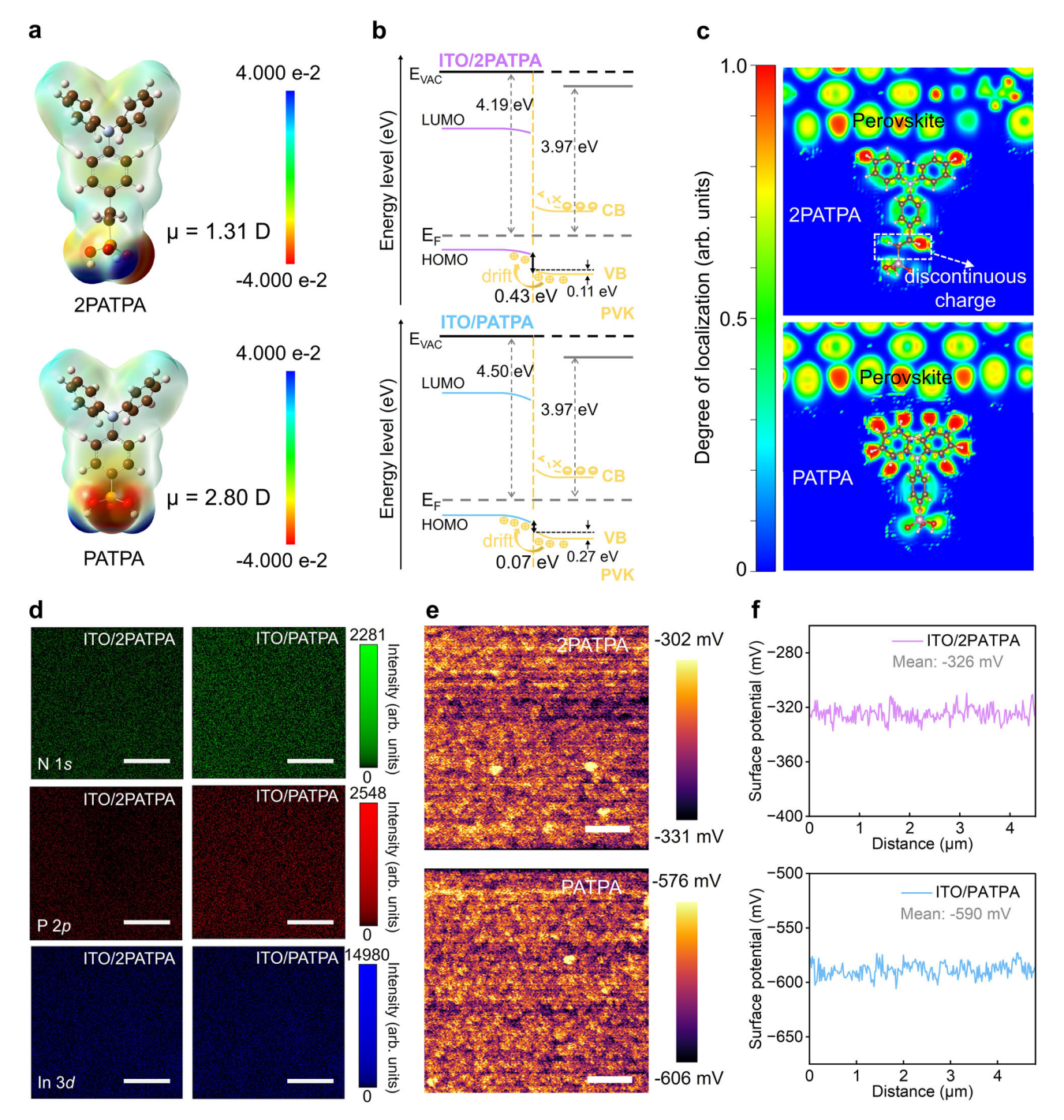


**Fig. 2** | **Characterization of SAMs modified ITO substrate. a** The electrostatic potential surfaces of 2PATPA and PATPA. **b** Energy levels obtained from the UPS results based on devices of ITO/2PATPA/PVK and ITO/PATPA/ PVK (The Band diagrams reference to the Fermi level ( $E_F$ ) and consider band bending at the interface). **c** ELF in the SAM molecular region on the perovskite surface. **d** XPS mapping

images of SAM molecules on ITO with scale bar of 50 nm. (In represents ITO, and N and P represent SAMs).  $\bf e$  The Kelvin probe force microscopy images of 2PATPA and PATPA with scale bar of 1  $\mu$ m.  $\bf f$  The contact potential difference image of 2PATPA and PATPA.

effectively minimized interfacial energy losses, thereby resulting in an enhanced  $V_{\rm OC}^{30,31}$ . Analysis of the ultraviolet visible (UV–Vis) absorption spectra for the SAM material solutions has revealed the optical band gaps, which helps with the determination of lowest unoccupied molecular orbit levels of PATPA (–2.06 eV) and 2PATPA (–1.26 eV) (Supplementary Fig. 19 and Supplementary Table 2). Additionally, the UV–Vis absorption spectra of perovskite films deposited onto ITO/2PATPA and ITO/PATPA substrates revealed a consistent bandgap of 1.55 eV, as depicted in Supplementary Fig. 20. As illustrated in Fig. 2b,

PATPA-modified ITO possesses a Fermi level of 0.31 eV deeper than that of 2PATPA-modified ITO, leading to improved VBM alignment and enhanced hole extraction efficiency<sup>32</sup>.

An electron localization function (ELF) analysis has uncovered that the incorporation of flexible alkyl chains leads to a disruption in the charge continuity within the HSL (Fig. 2c). Notably, 2PATPA molecules display pronounced discontinuities in the charge distribution across the flexible alkyl linker regions, which may impede the efficient transport of charges at the interface. On the other hand,

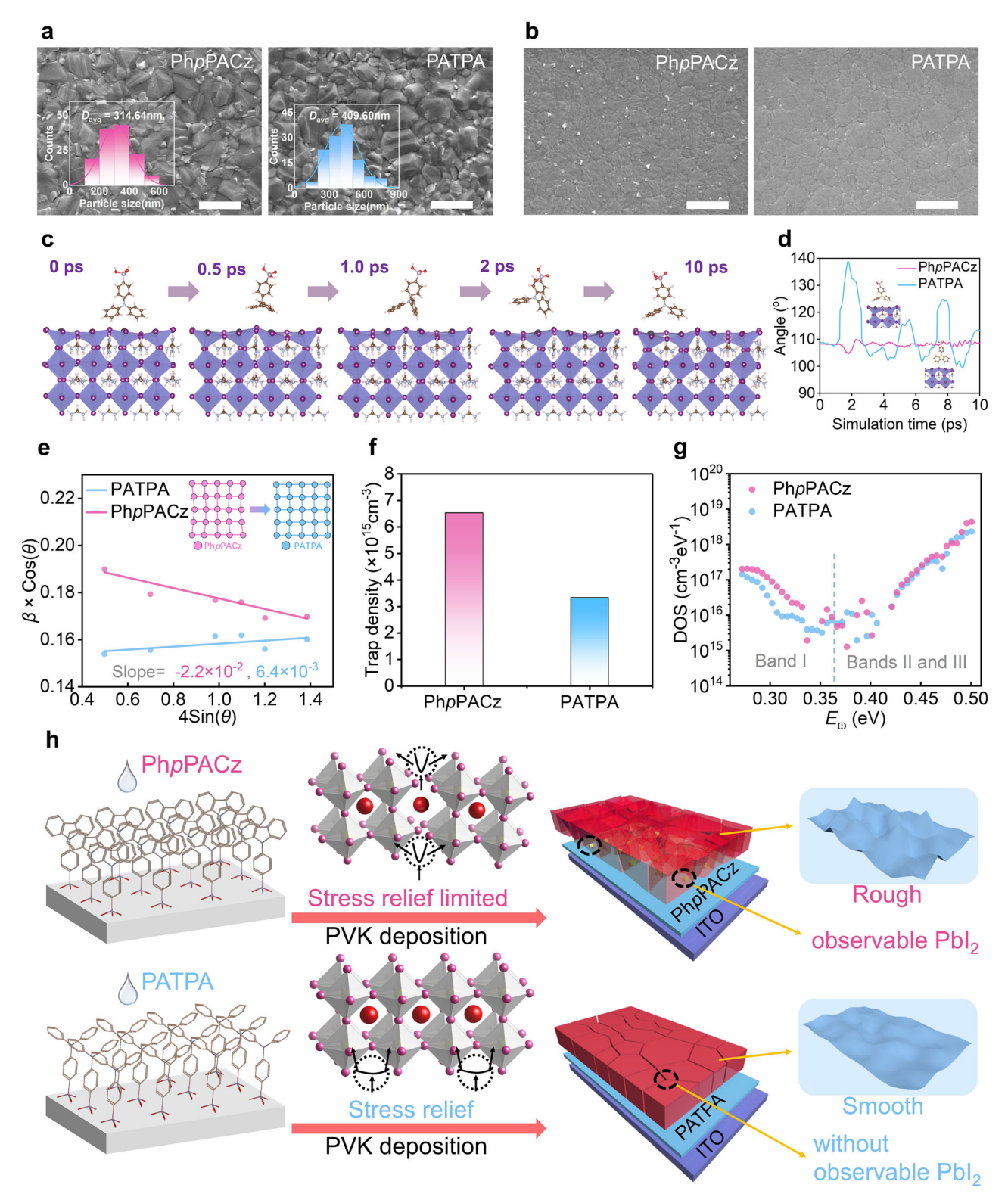


Fig. 3 | Characterization of perovskite deposited on SAMs. a Top-view SEM images and particle-size statistical distributions of perovskite films deposited on PhpPACz and PATPA (Scale bar 1  $\mu m$ ). b SEM images of the perovskite films peeled off from the PhpPACz and PATPA-modified substrates (scale bar 1  $\mu m$ ). c The molecular dynamics simulation trajectory of PATPA molecule on the perovskite

surface. **d** Angular evolution of SAM molecules on perovskite surface during AIMD simulations at 300 K. **e** Calculation of micro-strains in perovskite films based on PhpPACz and PATPA. **f** Trap density histogram extract from SCLC calculation results. **g** *t*-DOS plot of full devices. **h** Schematic diagram of morphology and defect passivation of perovskite films after deposition PhpPACz and PATPA, respectively.

PATPA molecules, characterized by phenyl linking groups, exhibit a more uniform and continuous charge distribution at the interface with the perovskite surface<sup>33,34</sup>. This continuity promotes a more effective in-plane transport of photoinduced charge carriers and improves their

subsequent transfer from the perovskite layer to the ITO substrate, thereby enhancing the overall device performance<sup>10</sup>.

The inclusion of flexible alkyl chains introduces challenges in achieving an optimal distribution for the HSL on the ITO surface. To

delve into this issue, XPS characterization was employed to assess the packing densities of PATPA and 2PATPA on the ITO substrate. Figure 2d illustrates that the signal intensities corresponding to N and P atoms for 2PATPA are notably lower than those for PATPA, which points to a higher packing density of PATPA molecules per unit area. XPS full-spectrum analysis (Supplementary Table 3) has uncovered that the phosphorus content on the ITO surface amounts to 0.45% for 2PATPA and 1.87% for PATPA, with corresponding nitrogen contents of 1.91% and 2.31%, respectively. The computed phosphorus-to-indium (P/ In) and nitrogen-to-indium (N/In) ratios for 2PATPA are 0.059 and 0.253, in contrast to 0.223 and 0.275 for PATPA, highlighting a marked disparity in packing density favoring PATPA. High-resolution XPS measurements (Supplementary Fig. 21) have enabled a more precise quantification of the spectral areas for nitrogen, phosphorus, and indium, further substantiating these findings. As detailed in Supplementary Table 4, the area ratios of N/In and P/In stand at 0.0344 and 0.0239 for 2PATPA, respectively, and 0.0432 and 0.0297 for PATPA, respectively. The CV measurements further confirmed the surface densities ( $\Gamma^*$ ) of 2PATPA and PATPA, as shown in Supplementary Fig. 22. The surface densities of 2PATPA and PATPA were determined to be  $1.39 \times 10^{13}$  molecules cm<sup>-2</sup> and  $1.86 \times 10^{13}$  molecules cm<sup>-2</sup>, respectively, indicating that the PATPA-modified ITO exhibits a higher packing density. These data confirm that PATPA achieves a substantially higher packing density on the ITO surface than 2PATPA, indicative of enhanced molecular coverage for effective interfacial modification.

Atomic force microscopy (AFM) and Kelvin probe force microscopy (KPFM) characterizations confirmed the role of molecular packing density in determining interfacial properties. A higher density of molecular packing is commonly associated with the development of smoother surface topographies, while the precise alignment of molecular structures is instrumental in minimizing contact potential differences (CPDs)<sup>10</sup>. Supplementary Fig. 23 illustrates that the root mean square (RMS) roughness values for ITO surfaces modified with 2PATPA and PATPA are 2.1 nm and 1.3 nm, respectively, underscoring the superior smoothness of the PATPA-modified ITO surface. Furthermore, KPFM measurements, as depicted in Fig. 2e, f, have quantified the surface potential of the SAM-coated ITO substrates. The CPD for the ITO/PATPA interface was markedly lower at -590 mV, in contrast to -326 mV for the ITO/2PATPA interface. This reduction in CPD suggests that the PATPA-modified ITO surface possesses a higher work function  $(W_F)$  and a more negative Fermi level, both of which are conducive to enhancing the device  $V_{\rm OC}$ . These observations are in harmony with the findings from UPS measurements<sup>35</sup>, thereby reinforcing the superiority of PATPA in the realm of interfacial engineering. Supplementary Fig. 24 provides the statistical distribution of CPD for the SAM molecules modifying ITO substrates. Notably, compared to the 2PATPA-modified ITO, the PATPA-modified samples exhibit a narrower surface potential distribution, indicating a more homogeneous surface potential.

Vertically aligned SAM molecules are capable of creating substrates with high-density, orderly arrays of HSL, thereby minimizing direct contact between the perovskite layer and the ITO. In corroborate this concept, scanning electron microscopy (SEM) was employed to examine the morphological characteristics of perovskite films deposited on ITO substrates modified with SAMs. Figure 3a and Supplementary Fig. 25 provide top-down SEM images along with grain size distribution analyses. The perovskite films grown on ITO/PATPA substrates showcased larger grain sizes, with an average diameter ( $D_{\rm avg}$ ) of 409.6 nm, in contrast to the  $D_{\rm avg}$  value of perovskite films grown on ITO/2PATPA substrate is 354.83 nm. Subsequent to peeling off the perovskite films, the morphology of the underlying interface was investigated (Fig. 3b and Supplementary Fig. 26). The perovskite films on PATPA-modified substrates were not only denser and more uniform but also exhibited a smoother surface texture compared with 2PATPA-

modified substrate. Furthermore, AFM images provided additional validation of these observations (Supplementary Fig. 27). In comparison to the perovskite films modified with 2PATPA, which exhibited an RMS roughness of 20.3 nm, the films modified with PATPA demonstrated a finer, more consistent crystalline structure, as evidenced by a decreased RMS value of 18.9 nm.

To ascertain the disparity in hole transport properties between 2PATPA and PATPA, single-carrier devices adopting the ITO/SAMs/Cu configuration were constructed for comparative analysis<sup>36</sup> (Supplementary Fig. 28). The results demonstrated that, compared to ITO/ 2PATPA substrates, devices based on PATPA exhibited improved Ohmic behavior, with the hole rectification ratio  $(K_{\text{hole}} = |J(-0.5 \text{ V})/$ J(+0.5 V)) reduced from 1.007 to 1.001 and the conductivity increased from 1.41 to  $2.35 \times 10^{-4}$  mS cm<sup>-1</sup>. The findings reveal an enhancement in hole selectivity at the ITO/PATPA interface, which consequently results in superior charge transport performance. Supplementary insights into the influence of different head groups, as observed in PhpPACz, are provided in the Supplementary Information. Supplementary Fig. 29 provides the energy level structure diagram of PhpPACz and perovskite laver. ELF analysis revealing a continuous charge distribution characteristic of PhpPACz on the perovskite surface (Supplementary Fig. 30). Furthermore, XPS mapping analysis (Supplementary Fig. 31) demonstrates that the packing density of PhpPACz on ITO surpasses that of 2PATPA, which is attributed to the presence of alkyl chains in the latter.

The AIMD simulations comparing PhpPACz and PATPA have elucidated that the TPA head group within PATPA possesses notable tilting and rotational flexibility (Figs. 1c and 3c). This adaptability in contact geometry enables a greater degree of interaction with the perovskite surface. Consequently, delving deeper into the impact of the PATPA molecular structure on perovskite film growth is imperative. To maintain a consistent basis for comparison, the part concentrated on PhpPACz and PATPA, which are differentiated solely by their head groups. Figure 3d illustrates the angular evolution of PATPA and PhpPACz molecules on the perovskite surface during a 10 ps AIMD simulation at 300 K. The C-N-C bond angle is defined as the torsional angle between the benzene rings in the SAM molecules. In PhpPACz, the torsional angle remains stable at approximately 110°, constrained by the C-C bond in the benzo-carbazole structure. In contrast, the triphenylamine structure of PATPA exhibits greater flexibility, with its two benzene rings showing opening and closing motions among 100-140° on the perovskite surface. Given that the SAM head group is the principal site of direct interaction with the perovskite, its structural configuration and mode of contact are instrumental in determining the crystalline growth of the perovskite matrix, as well as the morphology and quality of the buried interface, which is consistent with the SEM examination (Fig. 3a, b).

Furthermore, the contact angle for substrate modified with PATPA is 64°, which is larger than that of PhpPACz (56°) and 2PATPA (49°), as depicted in Supplementary Fig. 32. The higher contact angle associated with PATPA indicates a denser molecular packing on the ITO surface, resulting in a greater exposure of hydrophobic phenyl groups. This dense buried interface effectively isolates the perovskite from direct contact with ITO, which, in turn, improves film quality and reduced grain boundary defects. Furthermore, the SEM imaging revealed the presence of discrete, lustrous PbI2 solid precipitates within the perovskite films on PhpPACz substrates, albeit in minute quantities<sup>25</sup>. To delve deeper into this phenomenon, we peeled away the perovskite films and subjected the underlying interfaces to morphological analysis (Fig. 3b). The analysis revealed that although both sets of buried interfaces exhibited a dense and homogenous structure, the films coated on PATPA substrates presented with notably smoother surfaces, devoid of any discernible Pbl<sub>2</sub> precipitates. This suggests that PATPA enhances crystallization, reducing PbI<sub>2</sub> formation. DFT computation exhibited a notably

stronger adsorption affinity for PATPA, with an energy of -0.72 eV, much greater than the -0.38 eV observed for PhpPACz (Supplementary Fig. 33). Analysis via AFM has shown that perovskite films on PATPA-modified substrates had a smoother surface (18.9 nm roughness), compared to PhpPACz (21.4 nm) in Supplementary Fig. 27. Since the only structural difference between these two SAM molecules lies in their head groups, this finding highlights the superior ability of PATPA's TPA head group to facilitate better interfacial contact with the perovskite film.

The Williamson-Hall analysis, applied to the XRD patterns (Supplementary Fig. 34), served as a tool for assessing the quality of the perovskite films. The graphical representation of  $\beta\cos\theta$  plotted against  $4\sin\theta$ , as illustrated in Fig. 3e, provided insights into the films' strain distribution, with  $\beta$  denoting the peak width in relation to the  $2\theta$  angle, thereby elucidating the films' non-uniform strain attributes<sup>37–39</sup>. Figure 3e illustrates a pronounced reduction in residual strain, which plummeted from  $-2.2 \times 10^{-2}$  units in the PhpPACz-based films to a mere  $6.4 \times 10^{-3}$  units in the PATPA-based films. This improvement is attributable to the enhanced morphology of the underlying interface in the PATPA-modified perovskite layers. The increased crystallinity and diminished defects at this interface have successfully alleviated the residual stress, contributing to a more structurally stable film<sup>40-42</sup>. The TPA head groups of PATPA molecules are strategically aligned with the perovskite layer, effectively alleviating the compressive stress that arises at the interface between the perovskite film and the underlying substrate. This alignment leads to a reduction in non-uniform strain, thereby minimizing structural distortions within the Pb-I-Pb bond network, and promoting a more cohesive and stable perovskite film architecture<sup>43</sup>. Conversely, the reduced contact area between PhpPACz molecules and the perovskite layer hinders effective stress dissipation, resulting in localized stress accumulation. This phenomenon not only exacerbates the distortions in the Pb-I-Pb bond structure but also induces tilting of the PbI<sub>6</sub> octahedra, ultimately leading to the emergence of PbI<sub>2</sub> crystal defects within the film's lattice<sup>43,44</sup>. We further employed XPS to investigate their interfacial interactions (Supplementary Fig. 35). Compared to the pristine perovskite film, both PhpPACz and PATPA induced a shift of the Pb 4f and I 3d peaks toward lower binding energies. Notably, the peak shift caused by PATPA was more pronounced than that of PhpPACz. This indicates a stronger interfacial interaction and denser packing induced by PATPA, corroborating the improved structural integrity and reduced residual strain in the corresponding films.

To substantiate the adaptive nature of the PATPA head group in modulating contact properties, we conducted UV-vis absorption spectroscopy on ITO/PATPA and ITO/PhpPACz substrates at ambient temperature as well as under a range of thermal conditions (Supplementary Fig. 36). The spectroscopic analysis revealed that the UV-vis absorption profile of substrates treated with PhpPACz was impervious to the changes in environmental conditions. The substrates modified with PATPA displayed alterations in their UV-vis absorption, reflecting differences between the ambient and heated states. This observation implies that, as the perovskite film undergoes annealing, the unencumbered phenyl groups at the extremities of the TPA segment within PATPA experience configurational reorientation. Corresponding <sup>1</sup>H (Supplementary Fig. 36) and <sup>31</sup>P liquid-state nuclear magnetic resonance (NMR) (Supplementary Fig. 37) results, which showed hardly any observable changes before and after 85°C aging, confirmed this conclusion.

To ascertain the influence of SAM head groups on the quality of perovskite films and the dynamics of charge carriers at the SAM/PVK interface, we conducted a comprehensive analysis of steady-state photoluminescence (PL) and time-resolved photoluminescence (TRPL) spectra for films deposited on SAM-coated ITO substrates. The PL spectra (Supplementary Fig. 38) revealed that all perovskite films displayed a characteristic emission peak at 797 nm. Notably, the

perovskite film situated on the PATPA-modified substrate demonstrated an increase in photoluminescence intensity, suggesting a decrease in non-radiative recombination processes. Moreover, the augmented photoluminescence intensity was complemented by TRPL measurements, which elucidated that the perovskite film anchored on the PATPA-modified substrate exhibited the most prolonged carrier lifetime, reaching 2.38 µs. This is in contrast to the 2.31 µs observed for the film on the PhpPACz-modified substrate (Supplementary Fig. 39 and Supplementary Table 5). Such an extended carrier lifetime is indicative of increased grain sizes and an elevated level of crystalline quality in the perovskite films that have been nurtured on the SAMmodified surfaces<sup>45</sup>. Moreover, the PATPA-based perovskite film exhibited a shorter fast recombination time constant ( $\tau_1$ ) of 1.04 µs, which is substantially reduced compared to the 1.34 µs observed for the PhpPACz-based film. This discrepancy in recombination dynamics highlights that the PATPA-modified substrate possesses higher hole extraction efficiency<sup>46,47</sup>. Furthermore, we performed fluorescence lifetime imaging microscopy to evaluate the uniformity of carrier lifetimes and recombination dynamics across the perovskite films. As shown in Supplementary Fig. 40, the PATPA-modified perovskite films exhibit significantly improved homogeneity and extended PL lifetimes compared to those with PhpPACz.

Space-charge-limited current (SCLC) measurements, performed on hole-only devices under dark conditions, were utilized to ascertain the trap density within the perovskite films, as depicted in Supplementary Fig. 41. The trap-filled limit voltage  $(V_{TFI})$  for the PATPA-based devices was lower at 0.49 V, compared to the 0.96 V recorded for the PhpPACz-based devices. The computed trap density  $(N_t)$  for the PhpPACz-based devices was determined to be  $6.53 \times 10^{15}$  cm<sup>-3</sup>, whereas the PATPA-based devices exhibited a substantially lower  $N_t$  value of 3.33 × 10<sup>15</sup> cm<sup>-3</sup> (Fig. 3f). The decrease in trap density for the PATPAmodified substrates points to a marked enhancement in the quality of the interface between the perovskite layer and the bulk. The density of states (t-DOS) across the entire device architecture was measured (Fig. 3g). The shallow traps (Band I) were predominantly due to bulk impurities present within the perovskite layer. Conversely, the deep traps (Bands II and III) were attributed to surface defects, highlighting the distinct origins of trap states within the device<sup>48</sup>. The PATPA-based devices showcased a reduction by an entire order of magnitude in the t-DOS within the Band I region, when contrasted with the PhpPACzbased devices. Figure 3h schematically summarizes the morphological and defect passivation differences between perovskite films on ITO/ PhpPACz and ITO/PATPA substrates. Flexible, adaptive SAM head groups, as exemplified by PATPA, promote better interfacial contact, uniform film growth, and larger grain formation, in contrast to more rigid counterparts. The distinct effects associated with the linker groups in 2PATPA are discussed in detail in the Supplementary Information.

To examine the influence of SAM molecules, devices with the ITO/SAM/PVK/PDI/C<sub>60</sub>/BCP/Cu architecture were fabricated, as depicted in Fig. 4a. A SEM cross-sectional image of the device is provided in Supplementary Fig. 42 for structural insight. The devices performances were summarized in Supplementary Fig. 43 and Table 6, in which PATPA-based devices show the best photovoltaic performance and reproducibility compared to PhpPACz- and 2PATPA-based devices. Figure 4b, c shows the current-voltage (*J-V*) characteristics of the top-performing devices, utilizing three HSLs as detailed in Supplementary Table 7. The standout PATPA-modified device achieved an exceptional PCE of 26.21% during reverse scanning, with a  $V_{\rm OC}$  of 1.186 V, a  $J_{\rm SC}$  of 25.85 mA·cm<sup>-2</sup>, and a FF of 85.52%. The device's efficiency was officially certified at 26.26% with maximal power point tracking efficiency of 25.16%, as confirmed in Supplementary Fig. 44.

The external quantum efficiency (EQE) was precisely measured to calibrate the  $J_{SC}$ , which was found to be 25.18 mA·cm<sup>-2</sup>, as illustrated in

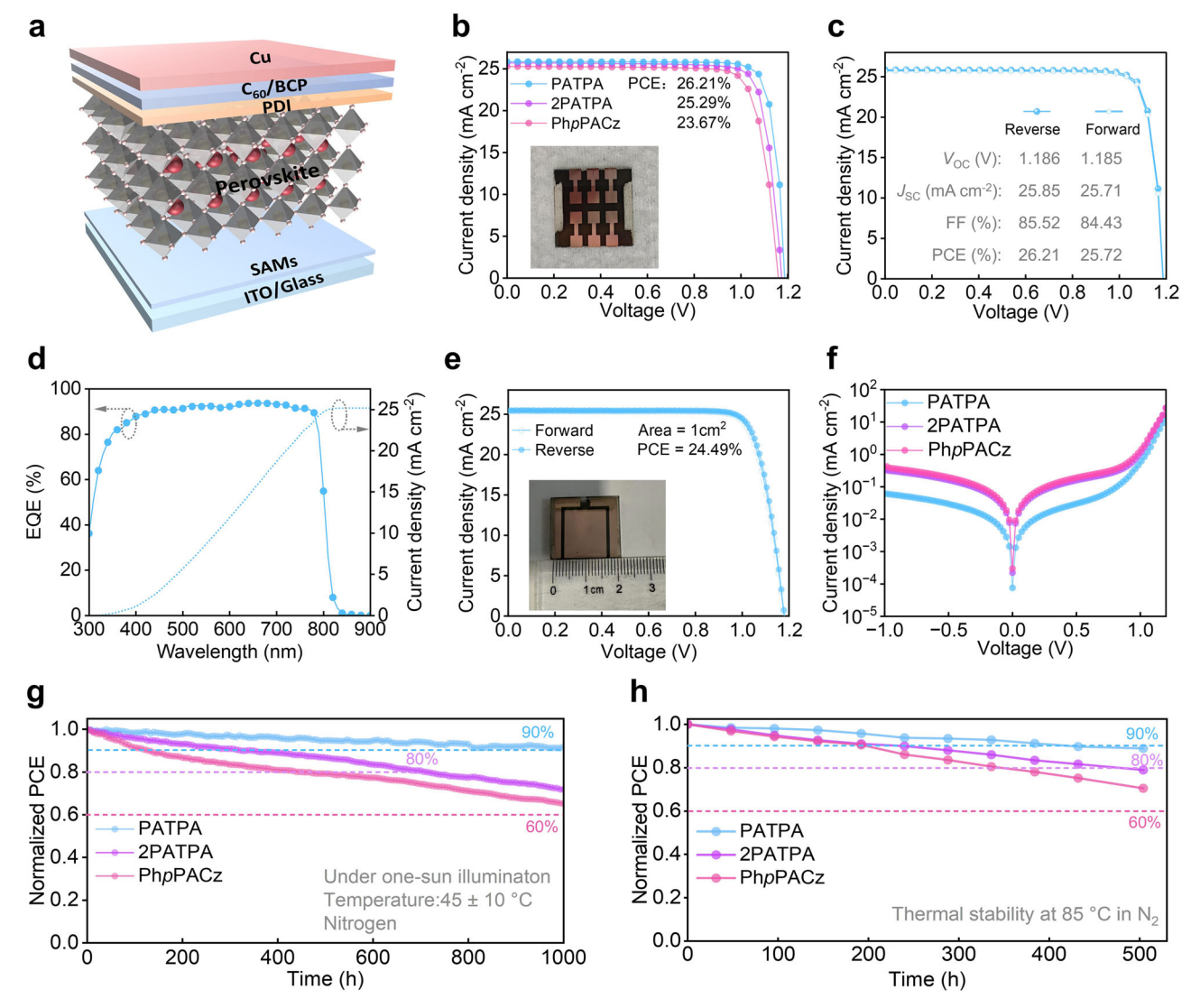


**Fig. 4** | **Configuration and performance of photovoltaic devices. a** The schematic of device architecture. **b** *J-V* curves of small area PSCs. **c** *J-V* curves of the best-performing device based on PATPA with different scan directions. **d** EQE spectrum of the champion device based on PATPA. **e** *J-V* characteristics of champion devices

based on PATPA with area = 1 cm². **f** Dark J-V curve of the PSCs. **g** Operational stability of device at maximum power point tracking under continuous light irradiation in N<sub>2</sub>. **h** Thermal stability of unencapsulated device under continuous heating at 85 °C in N<sub>2</sub>.

Fig. 4d, closely matching with the performance of the benchmark device. In order to assess the scalability of PATPA as a HSL for large-area applications, a device with an active area of 1 cm² was constructed as depicted in Fig. 4e, the large-area PATPA-based device achieved a PCE of 24.49% (with a  $V_{\rm OC}$  of 1.18 V,  $J_{\rm SC}$  of 25.46 mA·cm², and FF of 81.55%). In comparison, large-area devices using PhpPACz and 2PATPA as HSLs demonstrated PCEs of 22.11% and 23.52%, respectively (Supplementary Fig. 45 and Supplementary Table 8).

Supplementary Fig. 46 reveals that the PATPA-modified perovskite films displayed a distinct pattern of vertically aligned grains. This structural characteristic substantially mitigated non-radiative recombination, thereby markedly improving carrier extraction efficiency<sup>49</sup>. To delve further into the carrier dynamics within devices utilizing the three SAM molecules, electrochemical impedance spectroscopy (EIS) measurements were carried out. The utilized equivalent circuit model for EIS analysis is presented in Supplementary Fig. 47. The findings revealed that the recombination resistance ( $R_{\rm rec}$ ) for PhpPACz, 2PATPA, and PATPA devices were 21,701  $\Omega$ , 43,990  $\Omega$ , and 71,030  $\Omega$ , respectively, with the PATPA-based devices demonstrating the largest  $R_{\rm rec}$ . This outcome points to the efficacy of PATPA-modified devices in mitigating charge recombination. Additionally, the series

resistance ( $R_S$ ) exhibited a decline, dropping from 17.21  $\Omega$  for PhpPACz to 13.55  $\Omega$  for 2PATPA and further to 12.52  $\Omega$  for PATPA, as detailed in Supplementary Table 9. This reduction in  $R_S$  is indicative of an improved carrier collection efficiency in the PATPA devices<sup>29,45</sup>. Furthermore, to unravel the underlying mechanism of  $V_{\rm OC}$  loss, the Mott-Schottky technique was invoked to ascertain the built-in potential  $(V_{bi})$  and to determine the driving force responsible for the separation of photogenerated carriers (Supplementary Fig. 48). The analysis yielded that the  $V_{\rm bi}$  for the PATPA-based devices was notably higher at 0.94 V, in contrast to 0.82 V for the 2PATPA devices and 0.62 V for the PhpPACz devices. This elevated built-in potential serves as a robust impetus for the efficient separation of photogenerated carriers, concurrently mitigating non-radiative recombination and thereby enhancing the overall  $V_{\rm OC}$  of the devices<sup>35</sup>. This attribute is perfectly in synergy with the enhanced  $V_{\rm OC}$  recorded in the PATPAbased devices. The dark J-V curve depicted in Fig. 4f serves as additional confirmation of this finding. The PATPA-based devices demonstrated an exceptionally low dark current, and we calculated the rectification ratio (RR) of the devices under dark conditions at ±1 V. The RR values for PATPA, 2PATPA, and PhpPACz devices are 9.98, 3.62, and 3.36, respectively. The significantly enhanced RR in PATPA- modified devices indicates improved charge selectivity<sup>22</sup>, which is a strong testament to the effective suppression of interfacial non-radiative recombination, a key factor in optimizing the photovoltaic performance of the devices<sup>50</sup>.

The stable power output (SPO) of the devices was measured at the maximum power point (MPP), as illustrated in Supplementary Fig. 49. At a bias voltage of 1.05 V, the PATPA-based device sustained an output efficiency of 25.52% after 600 s of continuous illumination, outperforming the 24.18% of the 2PATPA-based device (bias voltage = 1.04 V) and the 23.03% of the PhpPACz-based device (bias voltage = 1.03 V). For long-term stability, devices with an ITO/SAM/ PVK/C<sub>60</sub>/SnO<sub>x</sub>/IZO/Cu architecture were tested under the ISOS-L-1I standard protocol. Over 1000 h in a nitrogen atmosphere, the PATPA-based device retained 91% of its initial PCE, while the 2PATPAbased and PhpPACz-based devices retained only 71% and 65%, respectively (Fig. 4g). Additionally, thermal stability was evaluated for the unencapsulated devices under nitrogen at 85 °C. Thermogravimetric analysis results (Supplementary Fig. 50) show that the decomposition temperature of PATPA (286 °C) is higher than those of 2PATPA (267 °C) and PhpPACz (277 °C), indicating that PATPA can withstand higher temperatures during annealing. Further film analysis, as shown in Supplementary Fig. 51, reveals minimal changes in perovskite films deposited on ITO/PATPA substrates after 300 h of aging, whereas films on ITO/PhpPACz substrates exhibit extensive white spot regions and the poorest perovskite film quality after 300 h. Corresponding XRD results (Supplementary Fig. 52) confirm these observations. PATPA-modified perovskite films retain weak Pbl<sub>2</sub> diffraction peaks after 300 h of aging, while 2PATPA- and PhpPACz-modified films display strong PbI<sub>2</sub> diffraction peaks after 100 h. The PhpPACz-modified films exhibit the strongest Pbl<sub>2</sub> diffraction intensity after 300 h, consistent with the largest and most numerous white spots observed on ITO/PhpPACz substrates. This discrepancy likely arises from differences in the crystallographic quality of perovskite films induced by distinct SAM modifications. Later, the stability of the unencapsulated devices were also tested. As shown in Fig. 4h, The PATPA-based device showed notable thermal stability, retaining 88% of its initial efficiency, better than the 78% and 70% retention observed for the 2PATPA-based and PhpPACz-based devices, respectively.

# **Discussion**

This research unveils the crafted design of the PATPA molecule, which thoughtfully pairs a flexible triphenylamine head group with a robust phenyl bridge. This structure is pitted against the performance of PhpPACz and 2PATPA, revealing a superior outcome. The findings confirm that PATPA's integrative design enhances the interfacial characteristics, resultant in a dense and defect-minimized interface with perovskite layers. This improved energy level alignment, hole extraction efficiency, and carrier transport. In a head-to-head comparison with PhpPACz, PATPA has been shown to alleviate lattice stress and curtail the formation of PbI<sub>2</sub> defects, which in turn promotes the development of larger grain sizes and more compact films. When measured against 2PATPA, PATPA's rigid linker group ensures a higher molecular packing density, fewer deep trap states, and reduces nonradiative recombination losses. Photovoltaic devices with PATPA have reached a maximum PCE of 26.21%, with larger-area devices (1 cm<sup>2</sup>) achieving a PCE of 24.49%. Stability tests show that PATPA-modified devices retain 91% of their initial efficiency after 1000 h of illumination and 88% after 500 h of thermal aging at 85 °C. This study heralds a design paradigm for non-substituted headgroup systems that masterfully blends the principles of flexibility and rigidity, offering valuable perspectives for the creation of SAM monolayers that are not only efficient but also stable, which is crucial for the advancement of photovoltaic technologies.

### Methods

#### **Materials**

The chemical reagents and solvents used for SAM molecules synthesis are all of reagent grade. 4-Bromotriphenylamine, palladium acetate [Pd(OAc)\_2], 1,1'-bis(diphenylphosphino)ferrocene (dppf), and potassium acetate (KOAc) were purchased from Bide Pharmatech Ltd. Diethyl phosphite, triethylamine (Et\_3N), and bromotrimethylsilane (TMSBr) were purchased from Energy Chemical Co. Ltd. Solvents and deuterium reagents were purchased from Adamasbeta Ltd. All materials are used without further purification unless otherwise noted.

For the materials used for PSCs fabrication included: ethanol (EtOH, 99.9%, Aladdin), isopropyl alcohol (IPA, 99.9%, Aladdin), N, N-dimethyl formamide (DMF, 99.8%, Aladdin), dimethyl sulfoxide (DMSO, 99.7%, Aladdin), chlorobenzene (CB, 99.9%, Aladdin), formamidinium iodide (FAI, >99.5%, Greatcell Solar Materials Pty. Ltd.), methylammonium iodide (MAI, >99.5%, Greatcell Solar Materials Pty. Ltd.), methylammonium chloride (MACl, >99.5%, Greatcell Solar Materials Pty. Ltd.), lead iodide (PbI<sub>2</sub>; 99.99%, TCI), 4-Methoxyphenylphosphonic Acid (95.0%, TCl), [4- (diphenylamino) phenyl) ethyl] phosphate (2PATPA, >98%, Xi'an Polymer Light Technology Crop), cesium iodide (CsI, >99.99%, Advanced Election Technology CO., Ltd), C<sub>60</sub> (99.99%, Xi'an Polymer Light Technology Corp.), bathocuproine (BCP, 99.99%, Xi'an Polymer Light Technology Corp.), Piperazine dihydriodide (PDI, 99.99%, Xi'an Polymer Light Technology Corp.), guanidine thiocyanate (GuaSCN, >99.5%, Xi'an Polymer Light Technology Corp.).

#### General characterizations of materials and thin film

<sup>1</sup>H NMR, <sup>13</sup>C NMR, and <sup>31</sup>P NMR spectra were recorded on Bruker AVANCE III 400 M. High-resolution electrospray ionization mass spectra were obtained from Thermo Scientific Q Exactive mass spectrometer, operated in heated electrospray ionization mode, and coupled with Thermo Scientific Ultimate 3000 system. CV was performed on CH Instruments Electrochemical Analyzer CHI760E using a three-compartment electrochemical cell, with samples in DMF containing 0.1 M [nBu<sub>4</sub>N]PF<sub>6</sub> as electrolyte and the ferrocene/ferrocenium (Fc/Fc<sup>+</sup>) as internal standard under scan rate of 0.1 V s<sup>-1</sup>. Ag/ AgCl, glassy carbon, and platinum wire were used as the reference electrode, working electrode, and counter electrode, respectively. UPS and XPS measurements were performed using an ultrahigh vacuum surface analysis system equipped with an ULVAC-PHI 5000 VersaProbe III spectrometer. UPS was performed with He I (21.22 eV) acting as the excitation source at an energy resolution of 50 meV. XPS and XPS mapping used monochromatic Al K radiation (1486.6 eV). All experiments were calibrated with respect to the Fermi edge of an atomically clean gold surface. SEM images were obtained by field emission SEM (JSM-7001F + DY-2000A). AFM images were captured by Multimode 8 (Bruker). X-ray diffraction (XRD) measurements were carried out using a D8 ADVANCE XRD spectrometer (Bruker) with a Cu K $\alpha$  line of  $\lambda = 1.5410$  Å. The steady photoluminescence (PL) spectra were obtained from the RF-6000 spectrofluorometer system with incident light at 480 nm and the TRPL was analyzed by the FLS 1000 fluorescence spectrometer equipped with a 450 nm excitation.

#### Preparation of perovskite precursor solutions for devices

The 1.5 M perovskite precursor solution with the composition of  $FA_{0.85}MA_{0.1}Cs_{0.05}Pbl_3$  was prepared by fully dissolving corresponding  $Pbl_2$ , FAl, MAl, and Csl in a mixed solvent of DMF and DMSO with a volume ratio of 4:1. 10 mg mL<sup>-1</sup> MACl and 4 mg mL<sup>-1</sup> GuaSCN were added in the solution for modified perovskite layer. The solution was stirred at room temperature until dissolved and filtered through a polytetrafluoroethylene filter (0.22  $\mu$ m) before use.

#### Fabrication of devices

ITO substrates  $(1.5 \times 1.5 \text{ cm}^2)$  were sequentially washed by detergent. deionized (DI) water, acetone, and isopropanol for 30 min through sonication method, respectively. Cleaned ITO substrates were treated with ultraviolet-ozone for 20 min, then the substrates were transferred into a nitrogen glovebox. SAM solutions are prepared by mixing 2 mmol of PhpPACz, 2PATPA, PATPA molecules and 0.02 mmol of (4-(3,6-Dimethoxy-9H-carbazol-9-yl) phenyl)phosphonic acid (OMe-PhpPACz, improved wettability) in 1mL ethanol, respectively. SAM solutions were spin-coated onto the ITO surface at 3000 rpm for 30 s, followed by annealing at 100 °C for 10 min. Then, 70 µL perovskite precursor solution was dropped onto ITO/SAMs substrates, spincoated at 1000 rpm for 10 s and 5000 rpm for 30 s. The 150 µL of chlorobenzene was poured on the substrates 10 s prior to the end of the program. Then, quickly transferred the substrates to annealing at 100 °C for 10 min. The supernatant of PDI saturated solution was spincoated at 5000 rpm for 30 s on the upper surface of the annealed perovskite films, and then transferred to a hot stage of 100 °C annealing for 5 min. Then, The C<sub>60</sub> (25 nm) and BCP (11 nm) were sequentially deposited on the perovskite films by vacuum evaporation. Finally, Cu (100 nm) was deposited as back electrode through a mask by thermal evaporation under  $6 \times 10^{-4}$  Pa.

#### **Device characterization**

The Keithley 2400 Source Measure Unit Instrument was used to test the current density versus voltage (*J-V*) curves and stabilized power output (SPO) and steady-state current density curves under AM 1.5 G, measure the conductivity and the space charge-limited current analysis under dark condition. Hole-only devices (ITO/SAMs/PVK/PTAA/Cu) were fabricated according to the PSC fabrication procedure. The solar cell quantum efficiency test system (Enlitech QE-R) was used to measure the EQE spectra of devices. The Mott–Schottky curves (MS) and the EIS were determined with the Chenhua CHI660E electrochemical workstation. The dark *J-V* characteristics of the hole-only devices were measured using a Keithley 2400 Source Meter. The long-term operational stability was conducted by applying the encapsulated devices under 1 sun equivalent LED lamp (3A) in N<sub>2</sub> environment. For thermal stability tests, every set of 6 unencapsulated devices was exposed to an 85 °C N<sub>2</sub> atmosphere and tested at 48-h intervals.

# Computational method

First-principles calculations based on DFT were conducted using the Vienna Ab Initio Simulation Package (VASP) under periodic boundary conditions. The ion-core electron interactions were described using the projector augmented wave method, and the exchange-correlation energy valence electrons was treated with the Perdew-Burke-Ernzerhof functional. A plane-wave cutoff energy of 400 eV was employed. To account for van der Waals interactions, Grimme's D3 dispersion corrections were applied. The energy convergence criterion for self-consistent field calculations during structural optimizations, including lattice parameters and internal atomic positions, was set to  $10^{-6}$  eV, and the maximum force convergence criterion was set to 0.02 eV Å-1.

Ab initio molecular dynamics (AIMD) simulations were performed to investigate the dynamic behavior of the SAM molecule on the ITO surface at room temperature. The ITO model was constructed by doping bulk  $\rm ln_2O_3$  with Sn atoms, and the (111) surface was selected as the most stable facet for the ITO model. The slab model was built using a  $1\times1\times1$  supercell of cubic  $\rm ln_2O_3$  (111), consisting of four O–In–O layers, with the bottom layer fixed to simulate bulk-like behavior. A vacuum layer of 20.0 Å was added along the [001] direction to prevent spurious interactions between periodic images. The final ITO slab dimensions were  $14.57\times14.57\times31.01\,\mbox{Å}^3$ .

To address the strong electron correlation effects associated with In-4d states, the DFT+U method was employed with a Hubbard U

parameter of 7 eV. Brillouin-zone sampling was restricted to the Gamma point for computational efficiency. For the upper perovskite model, the dimensions were  $19.47 \times 26.01 \times 42.26 \, \mathring{A}^3$ , including a  $20.0 \, \mathring{A}$  vacuum layer along the [001] direction to eliminate any artificial interactions between slabs.

#### **Reporting summary**

Further information on research design is available in the Nature Portfolio Reporting Summary linked to this article.

# **Data availability**

All data generated or analyzed during this study are included in the published article and its Supplementary Information. Additional data are available from the corresponding author on request. Source data are provided with this paper.

#### References

- Wang, Y. et al. Homogenized contact in all-perovskite tandems using tailored 2D perovskite. *Nature* 635, 867–873 (2024).
- National Renewable Energy Laboratory, U.S. Department of Energy. Best Research-Cell Efficiency Chart. https://www.nrel.gov/pv/cell-efficiency (USA, 2025).
- 3. Ding, Y. et al. Cation reactivity inhibits perovskite degradation in efficient and stable solar modules. *Science* **386**, 531–538 (2024).
- Li, M. L. et al. Self-assembled monolayers for interfacial engineering in solution-processed thin-film electronic devices: design, fabrication, and applications. Chem. Rev. 124, 2138–2204 (2024).
- Li, C. et al. Pros and cons of hole-selective self-assembled monolayers in inverted PSCs and TSCs: extensive case studies and data analysis. *Energy Environ. Sci.* 17, 6157–6203 (2024).
- Wu, T. et al. Self-assembled monolayer hole-selective contact for up-scalable and cost-effective inverted perovskite solar cells. Adv. Funct. Mater. 34, 2316500 (2024).
- Suo, J. et al. The dual use of SAM molecules for efficient and stable perovskite solar cells. Adv. Energy Mater. 15, 2400205 (2024).
- 8. Qu, G. et al. Self-assembled materials with an ordered hydrophilic bilayer for high performance inverted perovskite solar cells. *Nat. Commun.* **16**, 86 (2025).
- Isikgor, F. H. et al. Molecular engineering of contact interfaces for high-performance perovskite solar cells. *Nat. Rev. Mater.* 8, 89–108 (2022).
- Qu, G. et al. Conjugated linker-boosted self-assembled monolayer molecule for inverted perovskite solar cells. *Joule* 8, 2123–2134 (2024).
- Sangeeth, C. S. S., Jiang, L. & Nijhuis, C. A. Bottom-electrode induced defects in self-assembled monolayer (SAM)-based tunnel junctions affect only the SAM resistance, not the contact resistance or SAM capacitance. RSC Adv. 8, 19939–19949 (2018).
- Kong, G. D., Kim, M., Cho, S. J. & Yoon, H. J. Gradients of rectification: tuning molecular electronic devices by the controlled use of different-sized diluents in heterogeneous self-assembled monolayers. *Angew. Chem. Int. Ed.* 55, 10307–10311 (2016).
- Wang, Z., Lin, H. & Zhang, X. Revealing molecular conformation-induced stress at embedded interfaces of organic optoelectronic devices by sum frequency generation spectroscopy. Sci. Adv. 7, eabf8555 (2021).
- Park, S. et al. Thermoresponse of odd-even effect in n-alkanethiolate self-assembled monolayers on gold substrates. Chem. Eur. J. 29, e202203536 (2023).
- Kim, S. Y., Kang, H., Chang, K. & Yoon, H. J. Case studies on structure-property relations in perovskite light-emitting diodes via interfacial engineering with self-assembled monolayers. ACS Appl. Mater. Interfaces 13, 31236–31247 (2021).
- Perera, W. H. K. et al. Modification of hydrophobic self-assembled monolayers with nanoparticles for improved wettability and

- enhanced carrier lifetimes over large areas in perovskite solar cells. Sol. RRL 7, 2300388 (2023).
- Al-Ashouri, A. et al. Wettability improvement of a carbazole-based hole-selective monolayer for reproducible perovskite solar cells. ACS Energy Lett. 8, 898–900 (2023).
- Liu, S. et al. Buried interface molecular hybrid for inverted perovskite solar cells. Nature 632, 536–542 (2024).
- 19. Jiang, T. et al. Self-assembled monolayer hole transport layers for high-performance and stable inverted perovskite solar cells. *Energy Fuels* **38**, 21371–21381 (2024).
- Li, D. Y. et al. Co-adsorbed self-assembled monolayer enables highperformance perovskite and organic solar cells. *Nat. Commun.* 15, 7605 (2024).
- Kong, G. D. et al. Elucidating the role of molecule-electrode interfacial defects in charge tunneling characteristics of large-area junctions. J. Am. Chem. Soc. 140, 12303–12307 (2018).
- Yoon, H. J. et al. Rectification in tunneling junctions: 2,2'-bipyridyl-terminated n-alkanethiolates. J. Am. Chem. Soc. 136, 17155–17162 (2014).
- Zhang, S. et al. Minimizing buried interfacial defects for efficient inverted perovskite solar cells. Science 380, 404–409 (2023).
- Kim, S. Y., Cho, S. J., Byeon, S. E., He, X. & Yoon, H. J. Self-assembled monolayers as interface engineering nanomaterials in perovskite solar cells. Adv. Energy Mater. 10, 2002606 (2020).
- Liu, M. et al. Defect-passivating and stable benzothiophene-based self-assembled monolayer for high-performance inverted perovskite solar cells. Adv. Energy Mater. 14, 2303742 (2024).
- Jiang, W. L. et al. π-expanded carbazoles as hole-selective selfassembled monolayers for high-performance perovskite solar cells. Angew. Chem. Int. Ed. 61, e202213560 (2022).
- Bi, H. et al. All-perovskite tandem solar cells approach 26.5% efficiency by employing wide bandgap lead perovskite solar cells with new monomolecular hole transport layer. ACS Energy Lett. 8, 3852–3859 (2023).
- 28. Li, Z. et al. Stabilized hole-selective layer for high-performance inverted p-i-n perovskite solar cells. *Science* **382**, 284–289 (2023).
- Zhang, Z. H. et al. Anchoring charge selective self-assembled monolayers for tin-lead perovskite solar cells. Adv. Mater. 36, 2312264 (2024).
- Sun, A. X. et al. High open-circuit voltage (1.197 V) in large-area (1 cm²) inverted perovskite solar cell via interface planarization and highly polar self-assembled monolayer. Adv. Energy Mater. 14, 2303941 (2024).
- Park, S. M. et al. Low-loss contacts on textured substrates for inverted perovskite solar cells. *Nature* 624, 289–294 (2023).
- You, S. et al. Bifunctional hole-shuttle molecule for improved interfacial energy level alignment and defect passivation in perovskite solar cells. Nat. Energy 8, 515–525 (2023).
- Simeone, F. C. et al. Defining the value of injection current and effective electrical contact area for egain-based molecular tunneling junctions. J. Am. Chem. Soc. 135, 18131–18144 (2013).
- 34. Park, S., Kang, S. & Yoon, H. J. Power factor of one molecule thick films and length dependence. ACS Cent. Sci. 5, 1975–1982 (2019).
- 35. Li, C. et al. Fully aromatic self-assembled hole-selective layer toward efficient inverted wide-bandgap perovskite solar cells with ultraviolet resistance. *Angew. Chem. Int. Ed.* **63**, e202315281 (2024).
- Qu, G. et al. Enhancing perovskite solar cell performance through dynamic hydrogen-mediated polarization of nitrogen and sulfur in phthalocyanine. *Nano Energy* 118, 108974 (2023).
- Zheng, Z. et al. Pre-buried additive for cross-layer modification in flexible perovskite solar cells with efficiency exceeding 22%. Adv. Mater. 34, 2109879 (2022).
- Cheng, H. Y. et al. KBF<sub>4</sub> additive for alleviating microstrain, improving crystallinity, and passivating defects in inverted perovskite solar cells. Adv. Funct. Mater. 32, 2204880 (2022).

- 39. Du, Y. C. et al. Ionic liquid treatment for highest-efficiency ambient printed stable all-inorganic CsPbI<sub>3</sub> perovskite solar cells. *Adv. Mater.* **34**, 2106750 (2022).
- Liu, S. W. et al. Effective passivation with size-matched alkyldiam-monium iodide for high-performance inverted perovskite solar cells. Adv. Funct. Mater. 32, 2205009 (2022).
- Wang, H. et al. Interfacial residual stress relaxation in perovskite solar cells with improved stability. Adv. Mater. 31, 1904408 (2019).
- 42. Chang, X. Q. et al. Two-second-annealed 2D/3D perovskite films with graded energy funnels and toughened heterointerfaces for efficient and durable solar cells. *Angew. Chem. Int. Ed.* **62**, e202309292 (2023).
- Zhuang, X. et al. Trivalent Europium-Doped CsCl quantum dots for MA-free perovskite solar cells with inherent bandgap through lattice strain compensation. Adv. Mater. 35, 2302393 (2023).
- 44. An, Y. et al. Structural stability of formamidinium- and cesium-based halide perovskites. ACS Energy Lett. 6, 1942–1969 (2021).
- 45. Wu, J. et al. Bisphosphonate-anchored self-assembled molecules with larger dipole moments for efficient inverted perovskite solar cells with excellent stability. *Adv. Mater.* **36**, 2401537 (2024).
- Liu, Z. et al. Reducing perovskite/C<sub>60</sub> interface losses via sequential interface engineering for efficient perovskite/silicon tandem solar cell. Adv. Mater. 36, e2308370 (2023).
- 47. Wen, J. et al. Heterojunction formed via 3D-to-2D perovskite conversion for photostable wide-bandgap perovskite solar cells. *Nat. Commun.* **14**, 7118 (2023).
- 48. Zhu, P. et al. Aqueous synthesis of perovskite precursors for highly efficient perovskite solar cells. *Science* **383**, 524–531 (2024).
- 49. Jiang, W. L. et al. Spin-coated and vacuum-processed hole-extracting self-assembled multilayers with H-aggregation for high-performance inverted perovskite solar cells. *Angew. Chem. Int. Ed.* **63**, e202411730 (2024).
- 50. Yi, Z. et al. Achieving a high open-circuit voltage of 1.339 V in 1.77 eV wide-bandgap perovskite solar cells via self-assembled monolayers. *Energy Environ. Sci.* **17**, 202–209 (2024).

# Acknowledgements

This work was financially supported by the National Natural Science Foundation of China (62004089, 62374053, 22479071), the Major Program of Guangdong Basic and Applied Research Foundation (Nos. 2019B121205001), and the Special Zone Support Program for Outstanding Talents of Henan University. A.K.Y.J. thanks the sponsorship of the Lee Shau-Kee Chair Professor (Materials Science), and the support from the APRC Grants (9380086, 9610419, 9610440, 9610492, 9610508) of the City University of Hong Kong, the MHKJFS Grant (MHP/054/23) and MRP Grant (MRP/040/21X) from the Innovation and Technology Commission of Hong Kong, the Green Tech Fund (202020164) from the Environment and Ecology Bureau of Hong Kong, the GRF grants (11304424, 11307621, 11316422) and CRS grants (CRS\_CityU104/23, CRS\_HKUST203/23) from the Research Grants Council of Hong Kong, and the Guangzhou Huangpu Technology Bureau (2022GH02).

#### **Author contributions**

G.Q., S.C., A.K.Y.J., and Z.-X.X. conceived and designed the research. J.Y. and G.Q. carried out the fabrication and major characterization of IPSCs. Y.Q. conducted theoretical simulations. S.Y.C. synthesized and characterized the SAM molecules. J.H. and S.G. performed SEM, EIS, and MS measurements. Y.L. conducted the stability testing. Y.J. performed the SCLC measurements. N.S. contributed for drawing the schematic diagrams. S.C. and A.K.Y.J. contributed to the analysis and provided advice. G.Q., J.Y., Y.Q., and Z.-X.X. wrote the initial draft, and all authors contributed to the final paper.

#### **Competing interests**

The authors declare no competing interests.

# Additional information

**Supplementary information** The online version contains supplementary material available at https://doi.org/10.1038/s41467-025-62388-4.

**Correspondence** and requests for materials should be addressed to Geping Qu, Shi Chen, Alex K.-Y. Jen or Zong-Xiang Xu.

**Peer review information** *Nature Communications* thanks Feng Yan, and the other, anonymous, reviewer(s) for their contribution to the peer review of this work. A peer review file is available.

**Reprints and permissions information** is available at http://www.nature.com/reprints

**Publisher's note** Springer Nature remains neutral with regard to jurisdictional claims in published maps and institutional affiliations.

Open Access This article is licensed under a Creative Commons Attribution-NonCommercial-NoDerivatives 4.0 International License, which permits any non-commercial use, sharing, distribution and reproduction in any medium or format, as long as you give appropriate credit to the original author(s) and the source, provide a link to the Creative Commons licence, and indicate if you modified the licensed material. You do not have permission under this licence to share adapted material derived from this article or parts of it. The images or other third party material in this article are included in the article's Creative Commons licence, unless indicated otherwise in a credit line to the material. If material is not included in the article's Creative Commons licence and your intended use is not permitted by statutory regulation or exceeds the permitted use, you will need to obtain permission directly from the copyright holder. To view a copy of this licence, visit http://creativecommons.org/licenses/by-nc-nd/4.0/.

© The Author(s) 2025